Supplementary Information (SI) for Journal of Materials Chemistry B.

Supplementary Materials for

Architectural control of rod-coil block polypeptide thermoresponsive self-assembly via de novo design of coiled-coil orientation

Bin Wang *et al.*

*Corresponding author. Email: kiick@udel.edu

This PDF file includes:

Supplementary Text
Figs. S1 to S16
Tables S1 to S3

Supplementary Text

TABLE OF CONTENTS

Design of ELP-BFP sequences **3**
Fig. S1. DNA sequences of ELP-BFP constructs 3
Fig. S2. Amino acid sequences of ELP-BFP constructs 4
Table S1. Influence of guest residues of the ELP sequence on the ELP-BFP amphiphile transition temperature. 5

Characterization of Expressed ELP-BFP sequences **6**
Fig. S3. SDS-PAGE of purified ELP-BFP polypeptides 6
Fig. S4. MALDI MS analysis results for purified ELP-BFP polypeptides 7
Table S2. Amino acid analysis of V8-BFP sequences 8
Table S3. Expression yields for ELP-BFP sequences 9
Fig. S5. Turbidity results for His-V8-aBFP at different concentrations. 10
Fig. S6. Turbidity results for His-V8-pBFP at different concentrations 11
Fig. S7. Turbidity results for V8-aBFP-His at different concentrations 12
Fig. S8. Turbidity results for V8-pBFP-His at different concentrations 13
Fig. S9. (A) Sequence of ELP-BFP construction with N-terminal Histidine tag. (B) Summary of transition temperatures of different constructs. 14
Fig. S10. CD spectra of individual sequences and different constructs at different temperatures 15
Fig. S11. Cryo-TEM images for (A) His-V8-aBFP and (B) V8-aBFP-His 17
Fig. S12. Repetition of TEM images for (A) His-V8-pBFP, (B) V8-pBFP-His, (C) His-V8-aBFP, and (D) V8-aBFP-His 18
Fig. S13. Thickness distributions of different ELP-pBFP layers based on cryo-TEM images 19

ELP-BFP sequences simulation and data analysis **20**
Fig. S14. Simulation of ELP-BFP 20
Fig. S15. The residue density of (A) His-V8-aBFP, (B) V8-aBFP-His, (C) His-V8-pBFP, and (D) V8-pBFP-His 21
Fig. S16. The pair or radial distribution function (RDF) for His-V8-aBFP and V8-aBFP-His. 22
Fig. S17. The pair or radial distribution function (RDF) of His-V8-pBFP and V8-pBFP-His. 23
Fig. S18. Preliminary characterization via confocal microscopy under (A)fluorescence channel and (B) DIC channel of V8-pBFP-His, in the presence of the hydrophobic dye AZ488 24

ELP-BFP versatility **25**
Fig. S19. Transition temperatures of V8-aBFP-His under different solution conditions 25

Design of ELP-BFP sequences (Fig. S1, Fig. S2, Table S1).

His-A8-aBFP

ATGGGCCATCATCATCATCATCATCATCATCACAGCAGCGGCCATATCGACGACGACGACAAGCATATGCCCGGGGTACCCG
GAGCTGGAGTTCCAGGAGCAGGTGTCCCAGGCGCGGGCGTGCCGGGTGCGGGTGTGCCGGGCGCTGGCGTGCCGGGTGCGGGTG
TTCCGGGTGCCGGTGTTCCGGGTGCAGGCGTCGACCTCGAGGACGAGGAAATCCGTCGTATGGCGGAGGAAATTCGTCAGATGGC
GGAGCGTATCCAGCAAATGGCGGAACAAATTCAGCAAGAGGCGCTCGAGTAAGGATCC

His-A16-pBFP

ATGGGCCATCATCATCATCATCATCATCATCACAGCAGCGGCCATATCGACGACGACGACAAGCATATGCCCGGGGTACCAG
GAGCAGGAGTTCCCGGAGCTGGTGTCCCAGGCGCGGGGGTGCCGGGTGCAGGCGTCCCAGGCGCGGGTGTACCGGGTGCGGGCG
TTCCGGGCGCTGGCGTGCCGGGTGCAGGCGTGCCGGGTGCCGGTGTTCCGGGCGCGGGTGTTCCGGGTGCGGGCGTGCCGGGTGC
CGGTGTGCCTGGCGCTGGCGTTCCGGGTGCGGGTGTGCCGGGTGCTGGCGTTCCGGGTGCGGGTGTCGACCTCGAGTGCGACGAA
ATCATTAAGTACCTGGATCGTATCATTCGTCAGCTGGAGCGTATCATTCGTCAACTGGAGGAAATCATTAAACAGCTGCTCGAGTA
AGGATCC

His-F6-aBFP

ATGGGCCATCATCATCATCATCATCATCATCACAGCAGCGGCCATATCGACGACGACGACAAGCATATGCCCGGGGTACCAG
GTTTTGGAGTTCCCGGATTCGGGGTGCCAGGCTTCGGCGTTCCGGGTTTTGGCGTGCCGGGTTTTGGTGTTCCGGGTTTCGGCGTC
GACCTCGAGGACGAGGAAATCCGTCGTATGGCGGAGGAAATTCGTCAGATGGCGGAGCGTATCCAGCAAATGGCGGAACAAATT
CAGCAAGAGGCGCTCGAGTAAGGATC

His-F6-pBFP

ATGGGCCATCATCATCATCATCATCATCATCACAGCAGCGGCCATATCGACGACGACGACAAGCATATGCCCGGGGTACCAG
GTTTTGGAGTTCCCGGATTCGGGGTGCCAGGCTTCGGCGTTCCGGGTTTTGGCGTGCCGGGTTTTGGTGTTCCGGGTTTCGGCGTC
GACCTCGAGTGCGACGAAATCATTAAGTACCTGGATCGTATCATTCGTCAGCTGGAGCGTATCATTCGTCAACTGGAGGAAATCA
TTAAACAGCTGCTCGAGTAAGGATCC

His-V8-aBFP

ATGGGCCATCATCATCATCATCATCATCATCACAGCAGCGGCCATATCGACGACGACGACAAGCATATGCCCGGGGTACCCG
GAGTAGGTGTTCCAGGAGTCGGAGTCCCAGGCGTGGGCGTGCCGGGTGTTGGTGTTCCGGGTGTTGGCGTGCCGGGTGTTGGTGT
TCCGGGTGTGGGCGTGCCGGGTGTGGGCGTCGACCTCGAGGACGAGGAAATCCGTCGTATGGCGGAGGAAATTCGTCAGATGGC
GGAGCGTATCCAGCAAATGGCGGAACAAATTCAGCAAGAGGCGCTCGAGTAAGGATCC

His-V8-pBFP

ATGGGCCATCATCATCATCATCATCATCATCACAGCAGCGGCCATATCGACGACGACGACAAGCATATGCCCGGGGTACCCG
GAGTAGGTGTTCCAGGAGTCGGAGTCCCAGGCGTGGGCGTGCCGGGTGTTGGTGTTCCGGGTGTTGGCGTGCCGGGTGTTGGTGT
TCCGGGTGTGGGCGTGCCGGGTGTGGGCGTCGACCTCGAGTGCGACGAAATCATTAAGTACCTGGATCGTATCATTCGTCAGCTG
GAGCGTATCATTCGTCAACTGGAGGAAATCATTAAACAGCTGCTCGAGTAAGGATCC

V8-aBFP-His

CATATGAAGCTTGTTCCGGGTGTGGGCGTTCCGGGTGTGGGCGTTCCGGGTGTGGGCGTTCCGGGTGTGGGCGTTCCGGGTGTGG
GCGTTCCGGGTGTGGGCGTTCCGGGTGTGGGCGTTCCGGGTGTGGGCGTCGACCTCGAGGACGAGGAAATCCGTCGTATGGCGGA
GGAAATTCGTCAGATGGCGGAGCGTATCCAGCAAATGGCGGAACAAATTCAGCAAGAGGCGCTCGAGCACCACCACCACCACCA
CTGA

V8-pBFP-His

CATATGAAGCTTGTTCCGGGTGTGGGCGTTCCGGGTGTGGGCGTTCCGGGTGTGGGCGTTCCGGGTGTGGGCGTTCCGGGTGTGG
GCGTTCCGGGTGTGGGCGTTCCGGGTGTGGGCGTTCCGGGTGTGGGCGTCGACCTCGAGGACGAAATCATTAAGTACCTGGATCG
TATCATTCGTCAGCTGGAGCGTATCATTCGTCAACTGGAGGAAATCATTAAACAGCTGCTCGAGCACCACCACCACCACCACTGA

Fig. S1. DNA sequences of ELP-BFP constructs. The blue sequence highlighted indicates the His tag sequence from the plasmid.

His-A8-aBFP

MGHHHHHHHHHHSSGHIDDDDKHMPGVPGAGVPGAGVPGAGVPGAGVPGAGVPGAGVPGAGVDLEDEEIRRMAEEIRQMAERIQQMAEQIQQEALE

His-A16-pBFP

MGHHHHHHHHHHSSGHIDDDDKHMPGVPGAGVPGAGVPGAGVPGAGVPGAGVPGAGVPGAGVPGAGVPGAGVPGAGVPGAGVPGAGVPGAGVPGAGVDLECDEIIKYLDRIIRQLERIIRQLEEIIKQLLE

His-F6-aBFP

MGHHHHHHHHHHSSGHIDDDDKHMPGVPGFGVPGFGVPGFGVPGFGVPGFGVPGFGVDLEDEEIRRMAEEIRQMAERIQQMAEQIQQEALE

His-F6-pBFP

MGHHHHHHHHHHSSGHIDDDDKHMPGVPGFGVPGFGVPGFGVPGFGVPGFGVPGFGVDLECDEIIKYLDRIIRQLERIIRQLEEIIKQLLE

His-V8-aBFP

MGHHHHHHHHHHSSGHIDDDDKHMPGVPGVGVPGVGVPGVGVPGVGVPGVGVPGVGVPGVGVPGVGVDLEDEEIRRMAEEIRQMAERIQQMAEQIQQEALE

His-V8-pBFP

MGHHHHHHHHHHSSGHIDDDDKHMPGVPGVGVPGVGVPGVGVPGVGVPGVGVPGVGVPGVGVPGVGVDLECDEIIKYLDRIIRQLERIIRQLEEIIKQLLE

V8-aBFP-His

MKLVPGVGVPGVGVPGVGVPGVGVPGVGVPGVGVPGVGVPGVGVDLEDEEIRRMAEEIRQMAERIQQMAEQIQQEALEHHHHHH

V8-pBFP-His

MKLVPGVGVPGVGVPGVGVPGVGVPGVGVPGVGVPGVGVPGVGVDLEDEIIKYLDRIIRQLERIIRQLEEIIKQLLEHHHHHH

Legend for the amphiphile design:

MGHHHHHHHHHHSSGHIDDDDK or HHHHHH — His tag from plasmids (not inserted to the recombinant expression host)

$(VPGXG)_n$ — ELP

DEEIRRMAEEIRQMAERIQQMAEQIQQEA — aBFP

DEIIKYLDRIIRQLERIIRQLEEIIKQL — pBFP

Fig. S2. Amino acid sequences of ELP-BFP constructs

	$(VPGAG)_8$	$(VPGAG)_{16}$	$(VPGVG)_8$	$(VPGFG)_6$
aBFP	>85°C	-	35.0°C±2.0°C	<5°C
pBFP	-	>85°C	28.0°C±1.4°C	<5°C

Table S1.

Influence of guest residues of the ELP sequence on the ELP-BFP amphiphile transition temperature. The result is consistent with expectations and previous studies; alanine is more hydrophilic than valine and phenylalanine provides aromatic interactions that facilitate coacervation of ELP chains.[1,2] Multiple studies have shown that replacement of Val with Ala causes the transition temperature to increase with the extent of Ala substitution,[3] and our results indicate that this reduced propensity to associate could not be overcome with the fusion to a BFP oligomerization unit. The increasing aromatic content in the ELP sequence triggers the phase transition at a lower temperature,[4] and the attachment of the BFP was insufficient to maintain the solubility of the $(VPGFG)_x$-BFP constructs. The symbol (–) indicates that the specific sequence was not synthesized.

Characterization of Expressed ELP-BFP sequences (Fig. S3, Fig. S4, Table S2 and Table S3)

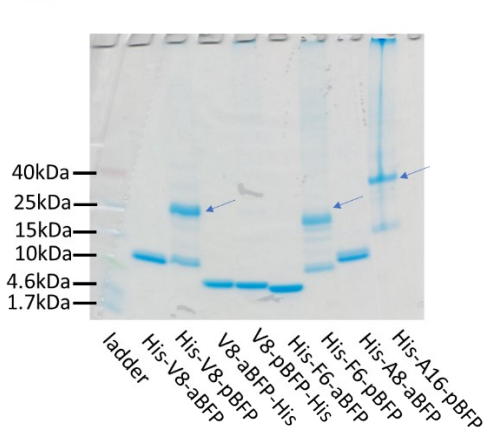

Fig. S3. SDS-PAGE of purified ELP-BFP polypeptides. The arrows indicate the potential presence of a dimer for His-ELP-pBFP due to the presence of Cys and the formation of disulfate bonds in BFP sequences. Similar dimer bands have been observed in the recombinantly expressed BFPs containing Cys.(1)

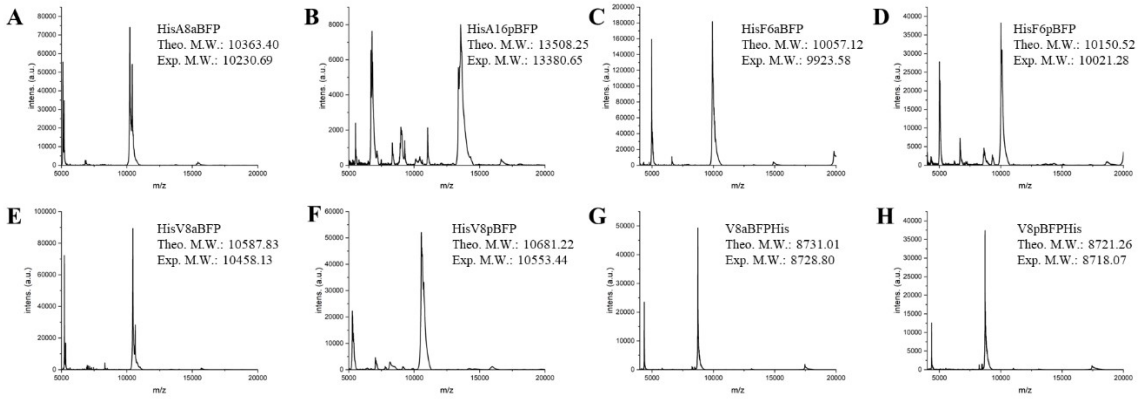

Fig. S4. MALDI MS analysis results for purified ELP-BFP polypeptides. The results indicate the dimer in His-ELP-pBFP observed in SDS PAGE was not observed in MALDI.

The molecular weight difference between the theoretical values and experimental values of the His-ELP-BFP sequences can be attributed to the self-digestion of the glutamic acid residue (M.W. = 129.13 Da) at the C-terminus as has been reported previously;(45) the shoulder in the mass spectrum may be an effect of the co-ionization of α-cyano-4-hydroxycinnamic acid which was used as the MALDI matrix.

Amino acid	His-V8-aBFP		His-V8-pBFP		V8-aBFP-His		V8-pBFP-His	
	Theo.	Exp.	Theo.	Exp.	Theo.	Exp.	Theo.	Exp.
Ala	3.96%	4.19%	0.00%	0.00%	4.76%	5.16%	0.00%	0.00%
Arg	3.96%	4.19%	3.96%	4.99%	4.76%	5.04%	4.82%	5.42%
Asx	5.94%	6.06%	6.93%	5.10%	2.38%	2.98%	3.61%	4.29%
Cys	0.00%	0.00%	0.99%	1.15%	0.00%	0.00%	0.00%	0.00%
Glx	14.85%	14.32%	8.91%	10.99%	17.86%	16.68%	10.84%	10.81%
Gly	18.81%	18.35%	18.81%	18.38%	19.05%	17.79%	19.28%	18.32%
His	11.88%	12.10%	11.88%	10.23%	7.14%	7.03%	7.23%	7.27%
Ile	4.95%	4.76%	8.91%	6.73%	4.76%	4.77%	9.64%	7.04%
Leu	1.98%	2.20%	5.94%	7.33%	3.57%	3.94%	8.43%	9.28%
Lys	0.99%	1.15%	2.97%	3.91%	1.19%	2.47%	3.61%	5.15%
Met	4.95%	4.76%	1.98%	1.53%	4.76%	5.17%	1.20%	1.21%
Phe	0.00%	0.52%	0.00%	0.00%	0.00%	0.00%	0.00%	0.00%
Pro	8.91%	8.50%	8.91%	8.93%	9.52%	9.32%	9.64%	8.81%
Ser	1.98%	1.92%	1.98%	2.41%	0.00%	0.00%	0.00%	0.00%
Thr	0.00%	0.18%	0.00%	0.00%	0.00%	0.00%	0.00%	0.00%
Trp	0.00%	0.00%	0.00%	0.00%	0.00%	0.00%	0.00%	0.00%
Tyr	0.00%	0.16%	0.99%	1.57%	0.00%	0.00%	1.20%	1.51%
Val	16.83%	16.64%	16.83%	16.76%	20.24%	19.65%	20.48%	20.88%
Nle	0.00%	0.00%	0.00%	0.00%	0.00%	0.00%	0.00%	0.00%
Sec	0.00%	0.00%	0.00%	0.00%	0.00%	0.00%	0.00%	0.00%

Table S2. Amino acid analysis of V8-BFP sequences.

Amino acid analysis of all expressed V8-BFPs confirms that the composition determined experimentally is generally within 5% of the expected values (Table S2). The His-V8-pBFP designs exhibit AAA results that are within 25% of the expected theoretical values, and were also observed to exhibit low-intensity, lower molecule weight peaks in the MALDI-MS analyses compared to the characterization data of other constructs (although the SDS PAGE of the His-V8-pBFP does not show any evidence of lower molecular weight products). In order to preliminarily assess the possible origins of these low-intensity peaks in the MALDI-MS results, the relative amino acid compositions of the amino acids in each domain (ELP and pBFP) were evaluated.

Evaluation of the relative ratios of the amino acids present only in the ELP domain illustrates that the ratio between Val, Pro, and Gly was ca. 2:1:2, suggesting the successful expression of the complete ELP domain. The appearance of these possible truncation products motivated the design of ELP-BFP constructs that carry the His tag on the C-terminus of the polypeptide; thus only full-length constructs are purified during the metal-ion affinity chromatography purification, which was confirmed by the characterization results.

Sample name	His-V8-aBFP	His-V8-pBFP	V8-aBFP-His	V8-pBFP-His
Yield (mg/L culture)	29.8±11.9	12.1±1.3	59.1±11.1	44.4±4.3

Table S3. Expression yields for ELP-BFP sequences. Averages and standard errors are calculated from two different synthetic batches. The results indicate the expression yield is influenced by the composition and order of the different domains in the ELP-BFP molecules.

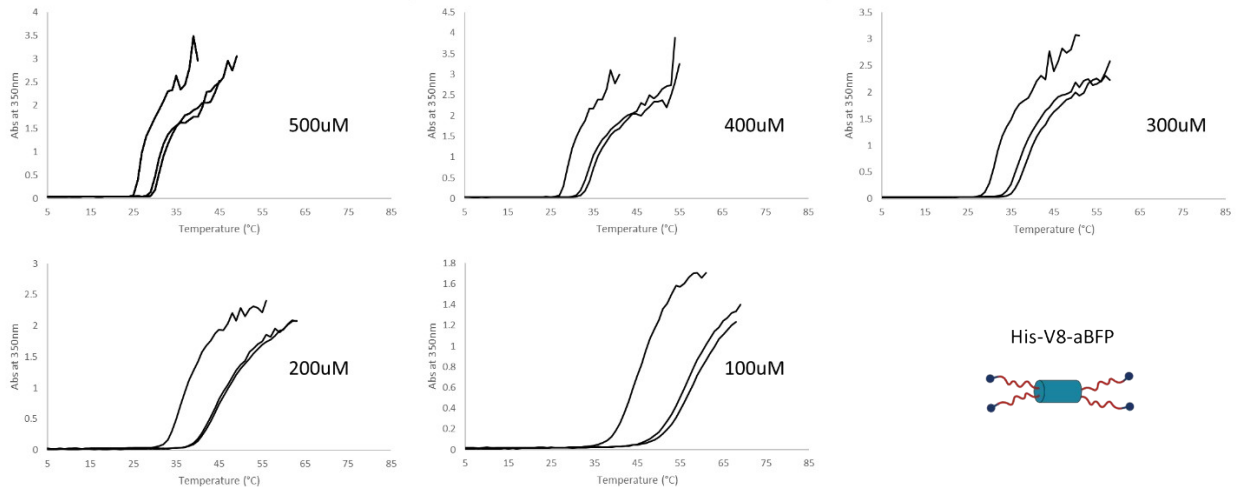

Fig. S5. Turbidity results for His-V8-aBFP at different concentrations.

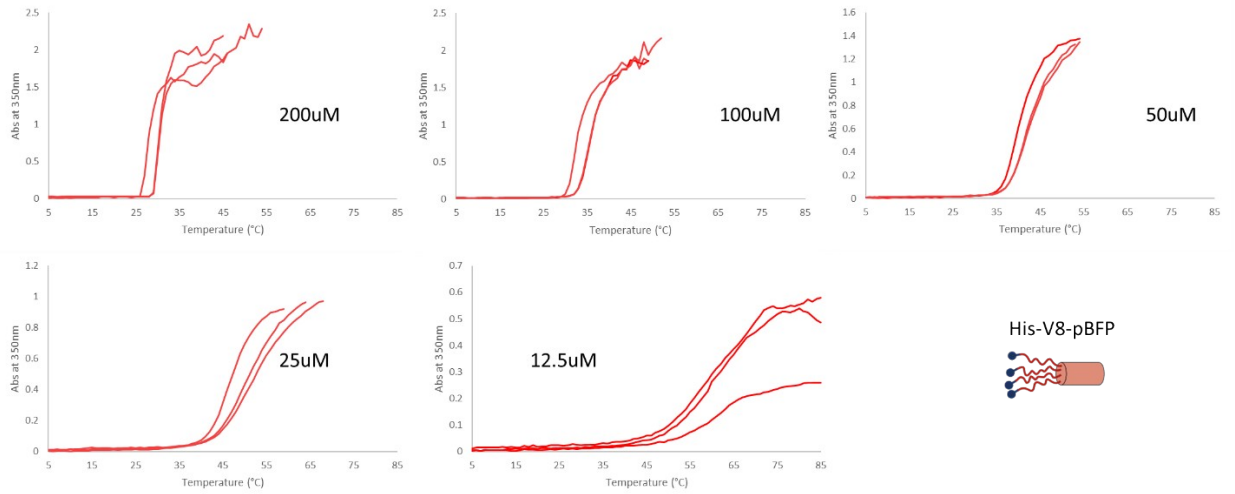

Fig. S6. Turbidity results for His-V8-pBFP at different concentrations.

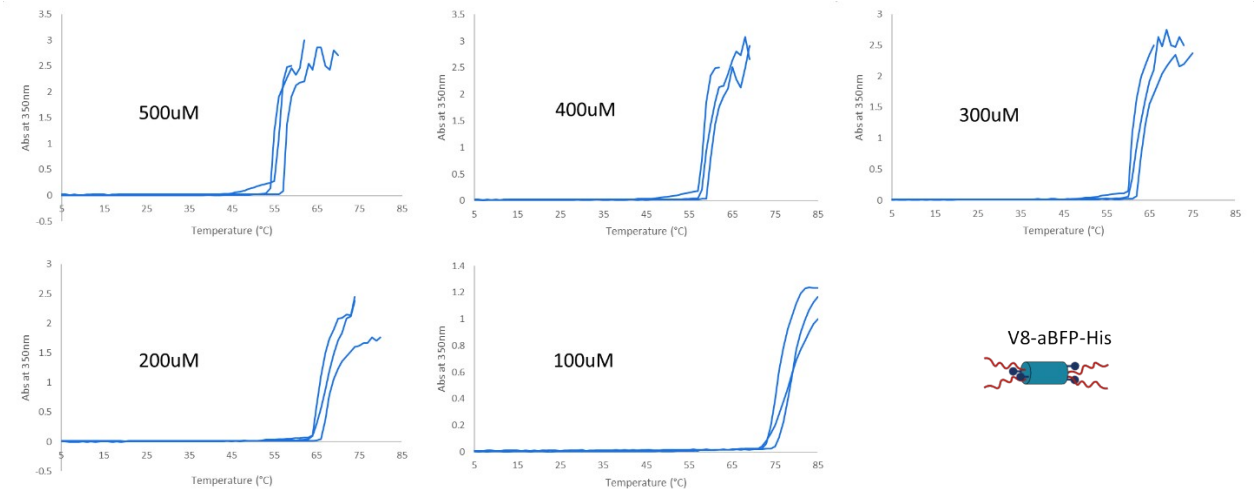

Fig. S7. Turbidity results for V8-aBFP-His at different concentrations.

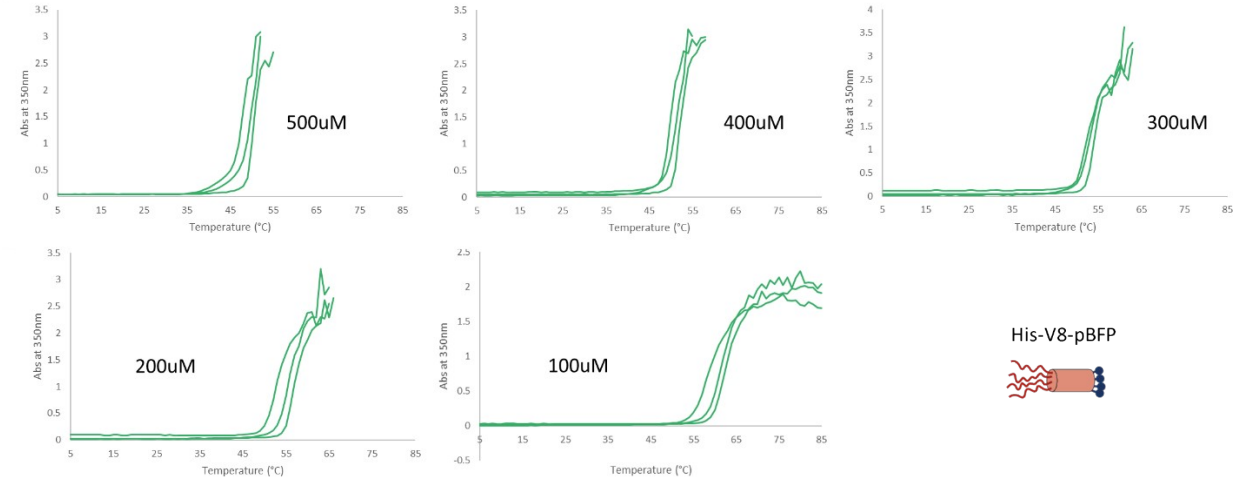

Fig. S8. Turbidity results for V8-pBFP-His at different concentrations.

A

ELP-aBFP with an N-terminal His6 tag (His6-V8-aBFP):
MHHHHHHKLVPGVGVPGVGVPGVGVPGVGVPGVGVPGVGVPGVGVPGVGVPGVGVDLEDEEIRRM
AEEIRQMAERIQQMAEQIQQEA
ELP-pBFP with an N-terminal His6 tag (His6-V8-pBFP):
MHHHHHHKLVPGVGVPGVGVPGVGVPGVGVPGVGVPGVGVPGVGVPGVGVPGVGVDLEDEIIKYLD
RIIRQLERIIRQLEEIIKQL)

B

Construct	Location of His-tag	n, His-tag length; His_n	Transition temperature, T_t
His6-V8-aBFP	N-terminus	6	39°C
His10-V8-aBFP	N-terminus	10	35°C
His6-V8-pBFP	N-terminus	6	34°C
His10-V8-pBFP	N-terminus	10	28°C
V8-aBFP-His6	C-terminus	6	61°C
V8-pBFP-His6	C-terminus	6	49°C

Fig. S9. (A) Sequence of ELP-BFP construction with N-terminal Histidine tag. (B) Summary of transition temperatures of different constructs.

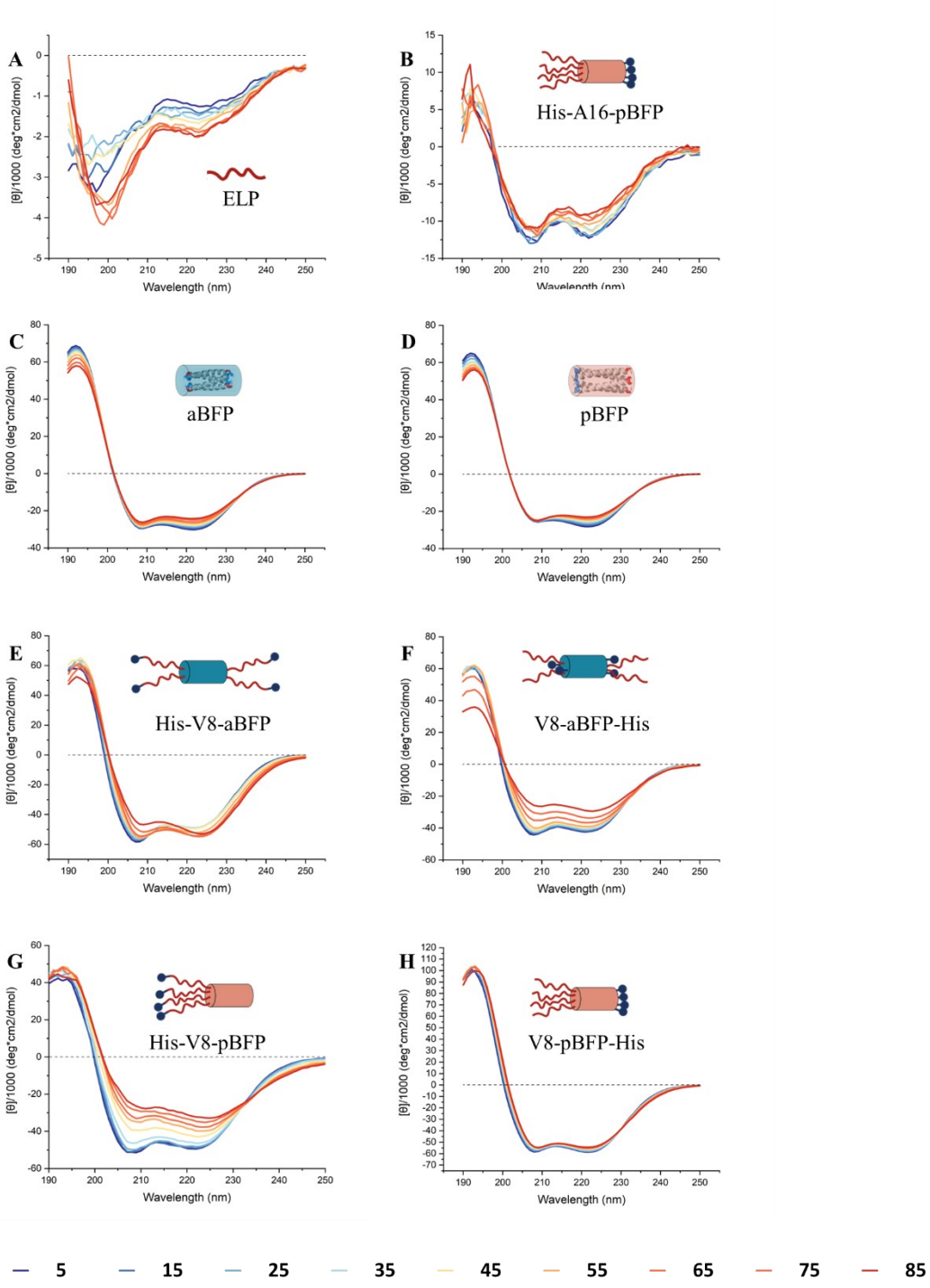

Fig. S10. CD spectra of individual sequences and different constructs at different temperatures. CD spectra for (A) His-A16 control, (B) His-A16-pBFP, (C) aBFP control, (D) pBFP control, (E) His-V8-aBFP, (F) His-V8-pBFP, (G) V8-aBFP-His, and (H) V8-pBFP-His at various temperatures indicates the stability of BFPs. The lower stability of pBFP in His-V8-pBFP compared to V8-pBFP-His is attributed to multiple factors including the different placement of the His-tag and ELP and the existence of a less stable truncation product. These results indicate that the α-helical signal arises mainly from the BFP domains in the ELP-BFP constructs. The BFPs remained helical at all temperatures in all constructs and

under all conditions investigated. A combination of the results from the MALDI-MS (Fig. S4) and amino acid analyses (Table S2) suggest that truncated pBFP is a possible impurity in the His-V8-pBFP samples; this small amount of truncated product will not eliminate coiled-coil formation, but may reduce the stability of the BFP domain slightly in these constructs.[5]

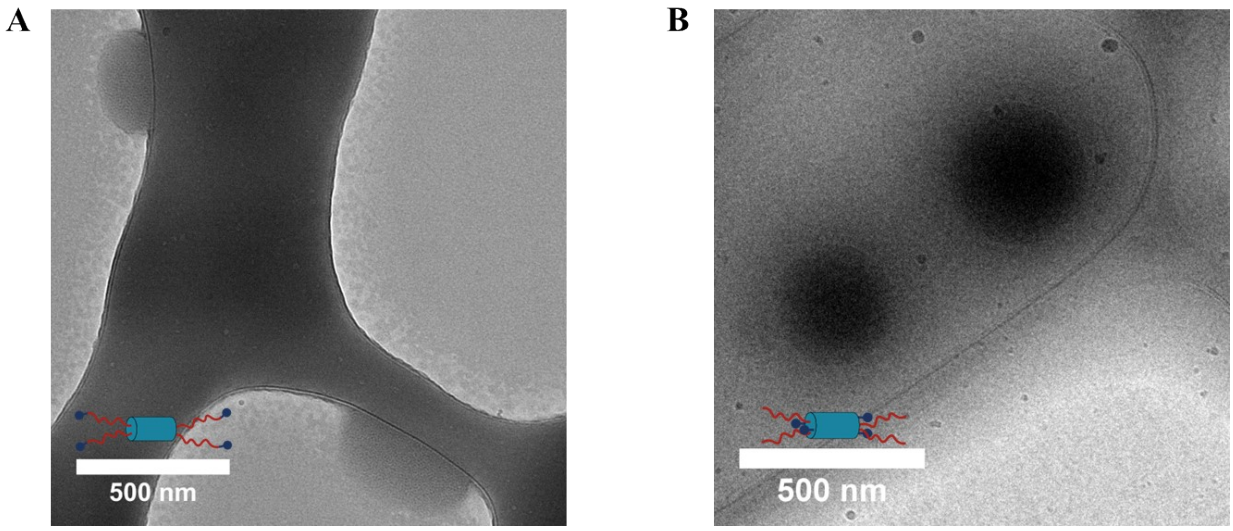

Fig. S11. Cryo-TEM images for (A) His-V8-aBFP and (B) V8-aBFP-His. The cryo TEM shows similar structures with similar dimensions as those in cast-film TEM studies, thus corroborating the formation of nanodroplets.

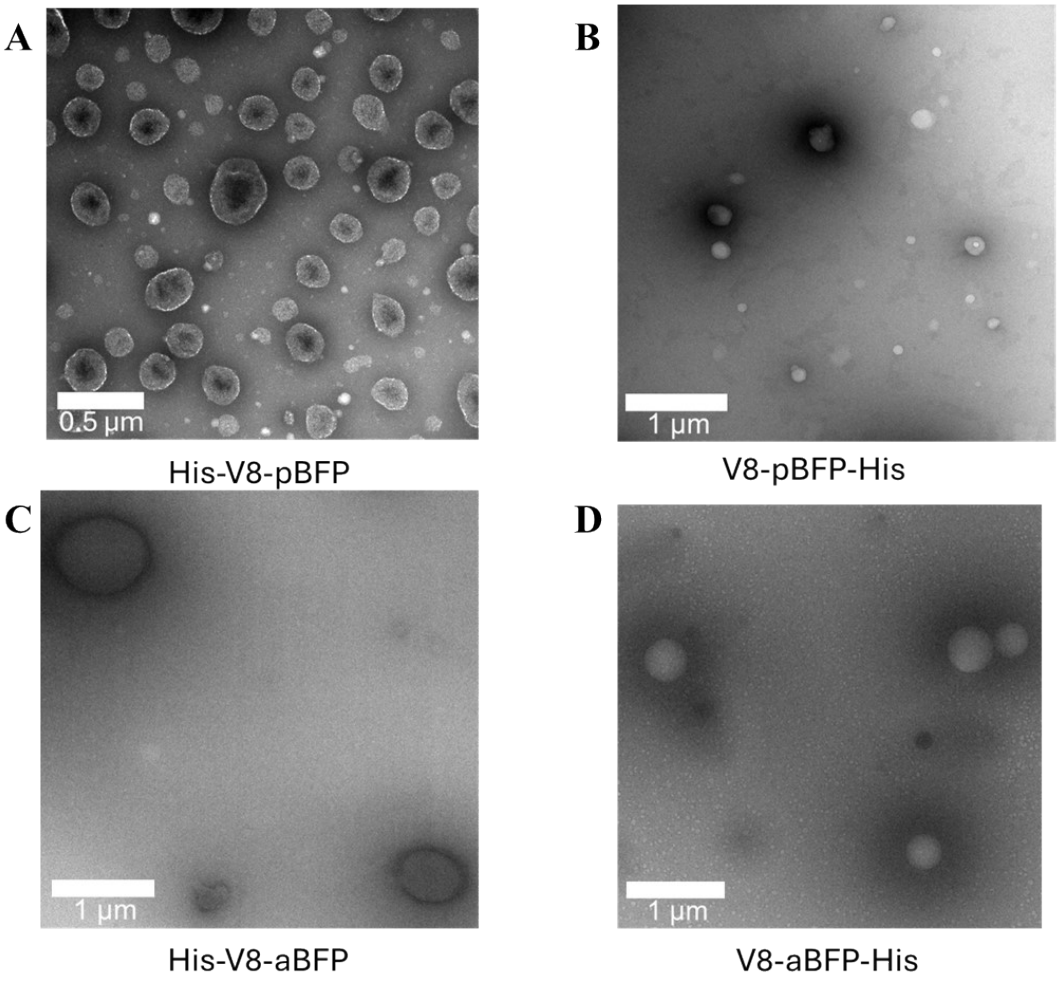

Fig. S12. Repetition of TEM images for (A) His-V8-pBFP, (B) V8-pBFP-His, (C) His-V8-aBFP, and (D) V8-aBFP-His. The peptide samples and TEM grids were prepared separately from the samples shown in the manuscript.

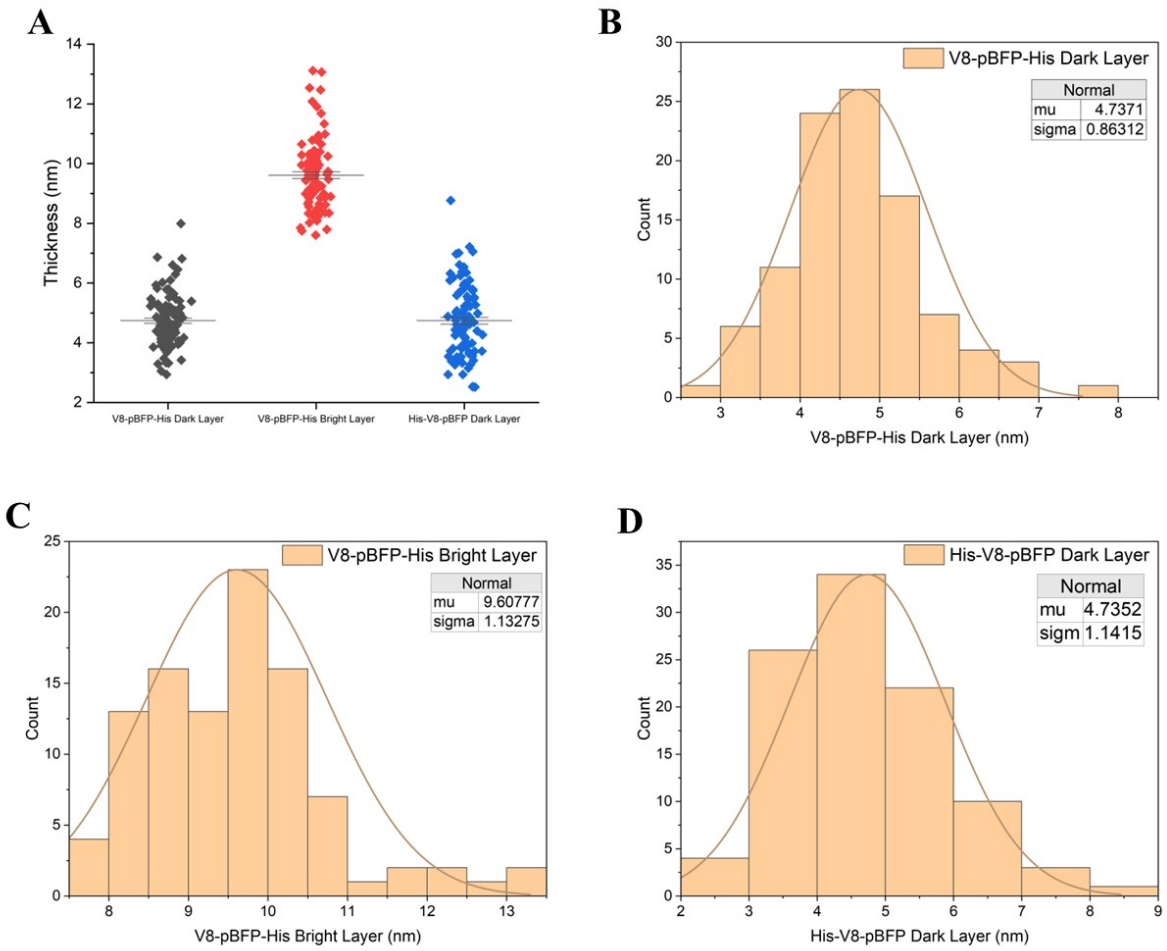

Fig. S13. Thickness distributions of different ELP-pBFP layers based on cryo-TEM images. (A) Layer thickness comparation between different layers. (B) Distribution of V8-pBFP-His dark layer (ELP layer) (B) Distribution of V8-pBFP-His bright layer (BFP layer) (B) Distribution of His-V8-pBFP dark layer (ELP layer). ELP layer thickness was similar in His-V8-pBFP (4.7±1.1nm) and V8-pBFP-His (4.7±0.9nm). The results suggest that the assembly of the ELP-BFP constructs into bilayers was similar but that the location of the His tag supports assembly into a different nanoscale morphology. Detailed methods can be found in the Cryo-TEM section of the Experimental Methods.

ELP-BFP sequences: simulation and data analysis (Fig. S14, Fig. S15, Fig. S16 and Fig. S17)

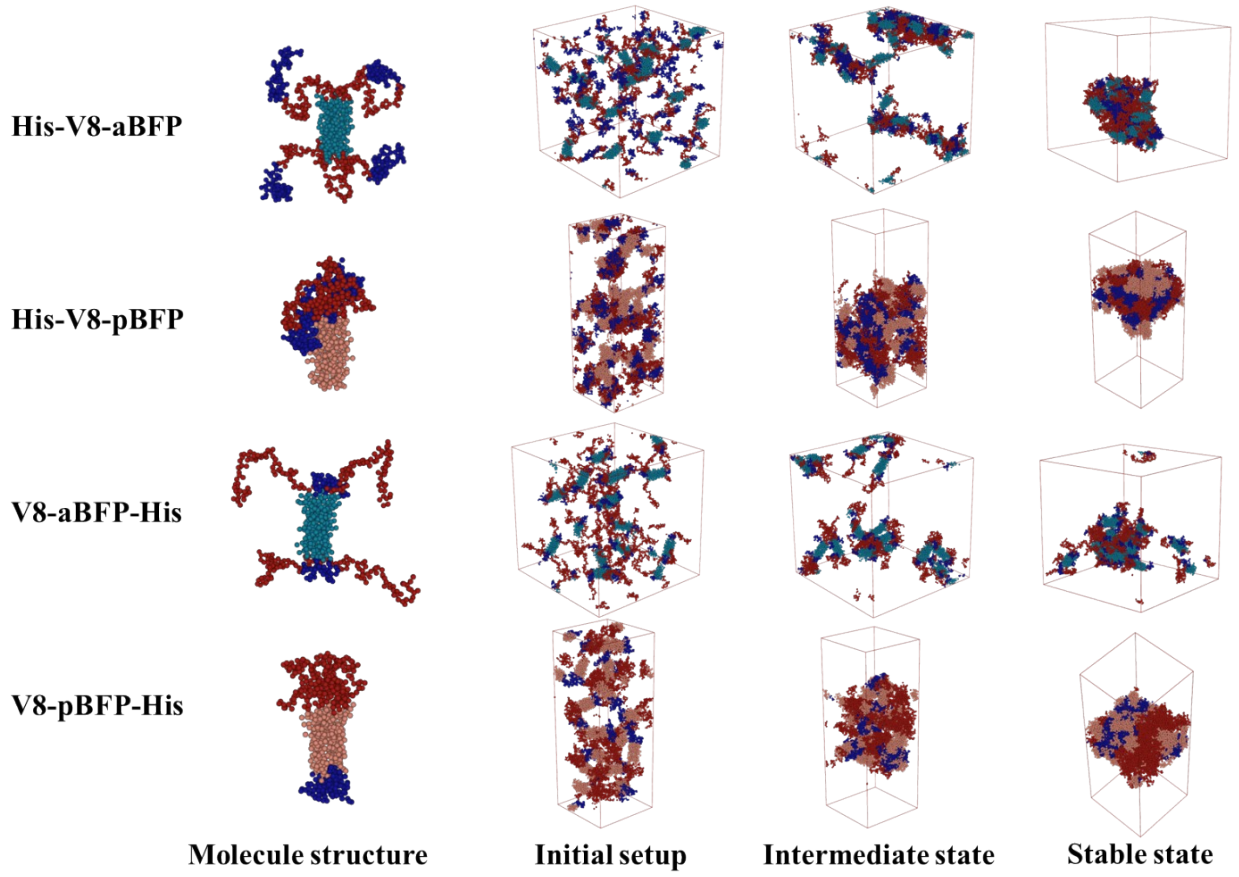

Fig. S14. Representative configurations sampled from simulations of ELP-BFP constructs. Dark blue, dark red, and cyan-blue, and pink chains in represent the sequence segments of His-tag, ELP, aBFP, and pBFP, respectively; the coloring scheme is the same as that of Fig. 1. The molecules were placed randomly in the simulation box at the start of the simulations. The co-localization of the ELP beads (dark red) at elevated 'temperature' indicates that aggregation of ELP drives assembly.

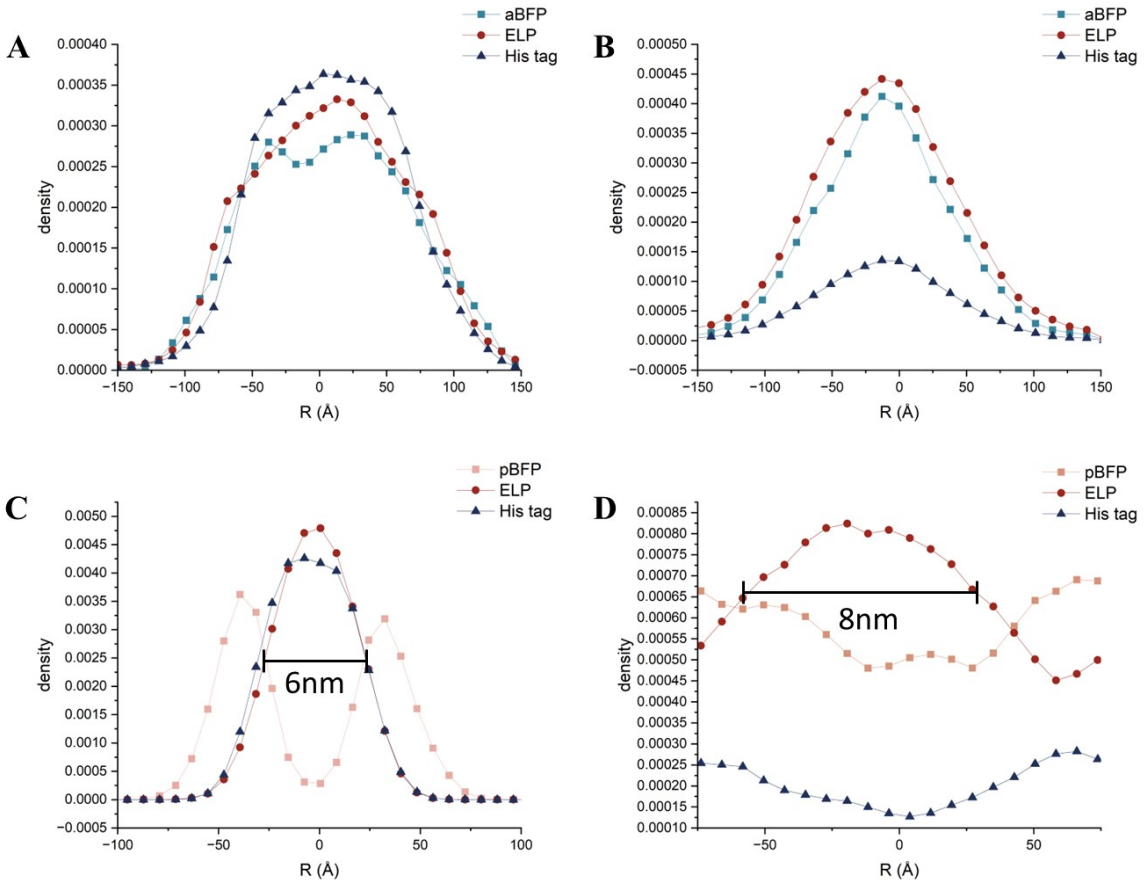

Fig. S15. The residue density of (A) His-V8-aBFP, (B) V8-aBFP-His, (C) His-V8-pBFP, and (D) V8-pBFP-His. Density of coarse-grain beads of the indicated type are presented as a function of the linear dimension within the simulation box, where the linear dimension is chosen to be perpendicular to lamellar structures observed in (C) and (D). For (A) and (B), the z coordinate of the simulation box was chosen as the linear direction. (A) His-V8-aBFP and (B) V8-aBFP-His show colocalization of ELP, aBFP, and the His tag. (C) His-V8-pBFP shows colocalization of ELP and His tag in one layer and pBFP positioned in another separate layer. The thickness of the ELP layer is approximately 6nm. (D) V8-pBFP-His also shows a layered structure, but with colocalization of pBFP and His tag in one layer and ELP in a separate layer. The thickness of the ELP layer estimated from these simulations is approximately 8nm. For the density calculations, the non-water beads were centered in the simulation box along the linear dimension based on their center of mass. Then, the simulation box was divided into bins along the linear dimension, with a bin size of about 5–10 nm. The number of non-water beads were counted corresponding to each protein segment within each bin and this count was divided by the volume of the bin to obtain the density for each residue bead type. R represents the distance from the center of the simulation box along the corresponding linear dimension.

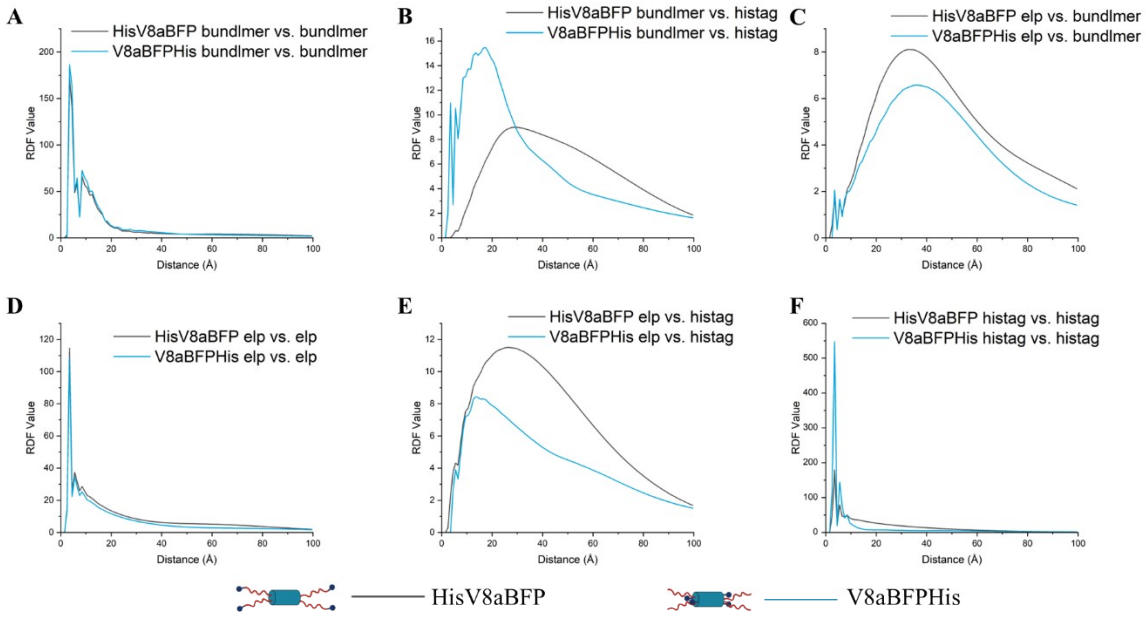

Fig. S16. The pair or radial distribution function (RDF) value for His-V8-aBFP and V8-aBFP-His. The differences between the two constructs are attributed to the different placement of the His tag in the different ELP-BFP constructs. The data in Fig. S16B yields peaks at closer distances for His-tag/BFP pairs with V8-aBFP-His than for His-V8-aBFP. Fig. S16F indicates peaks for short separations (less than 10Å) between His tags, consistent with their close contact. The pair distribution function indicates there is little significant difference the distributions of pair distances for BFP-BFP (Fig. S16A), ELP-BFP (Fig. S16C), and ELP-ELP (Fig. S16D). In each case, the pair distribution function is calculated only using distances between the corresponding coarse-grain beads within distinct, separate tetrameric bundlemer-based assemblies; intra-tetramer distances between beads are not considered.

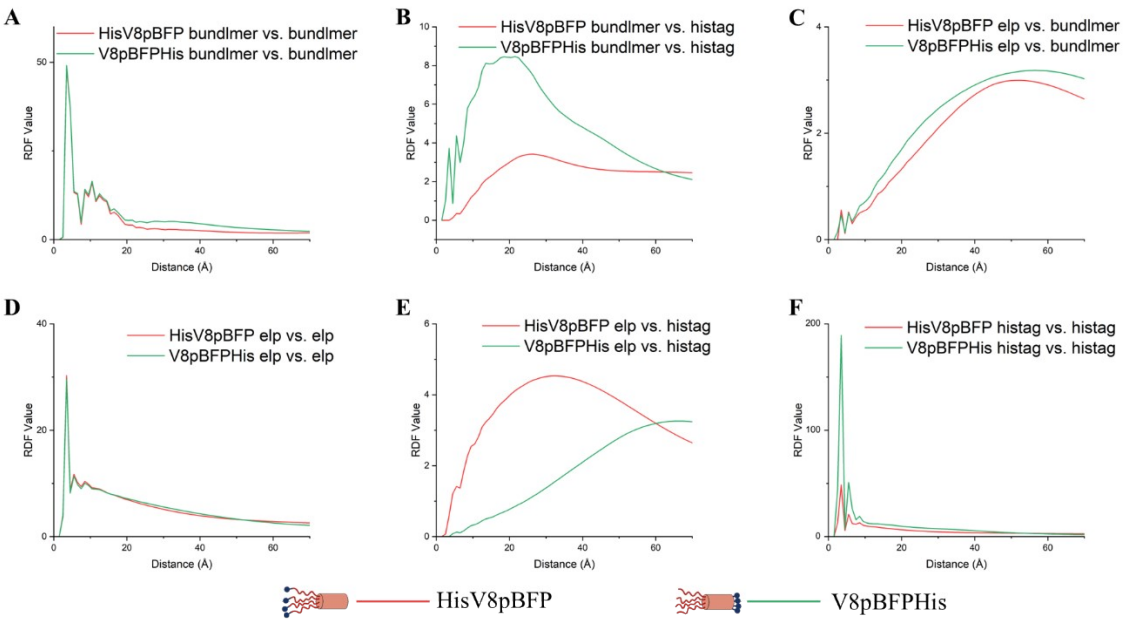

Fig. S17. The pair or radial distribution function (RDF) of His-V8-pBFP and V8-pBFP-His. Little difference in the distribution functions is observed for residue beads on distinct bundles for BFP-BFP (Fig S17A), ELP-BFP (Fig. S17C) and ELP-ELP (Fig. S17A). From Fig S17B, bundle (BFP) beads of V8-pBFP-His are in closer proximity (larger amplitude at smaller distances) to His tag beads on other tetramers than observed for His-V8-pBFP. Fig. S17E indicates that ELP is in much closer proximity to His tag units in His-V8-pBLP than for V8-pBFP-His; this observation is consistent with partial sequestration of the His tag from ELP. Fig S17F indicates larger amplitude and larger numbers of His tag residues in close proximity (less than 10 Å) for V8-pBFP-His as compared to His-V8-pBFP. Data in (B), (E), and (F) are consistent with partial bilayer formation (Fig. 6B), wherein His tag residues are sequestered at the interface between bilayer leaflets. Pair distributions are calculated using only distances between residues in distinct tetrameric units, as in Fig S16.

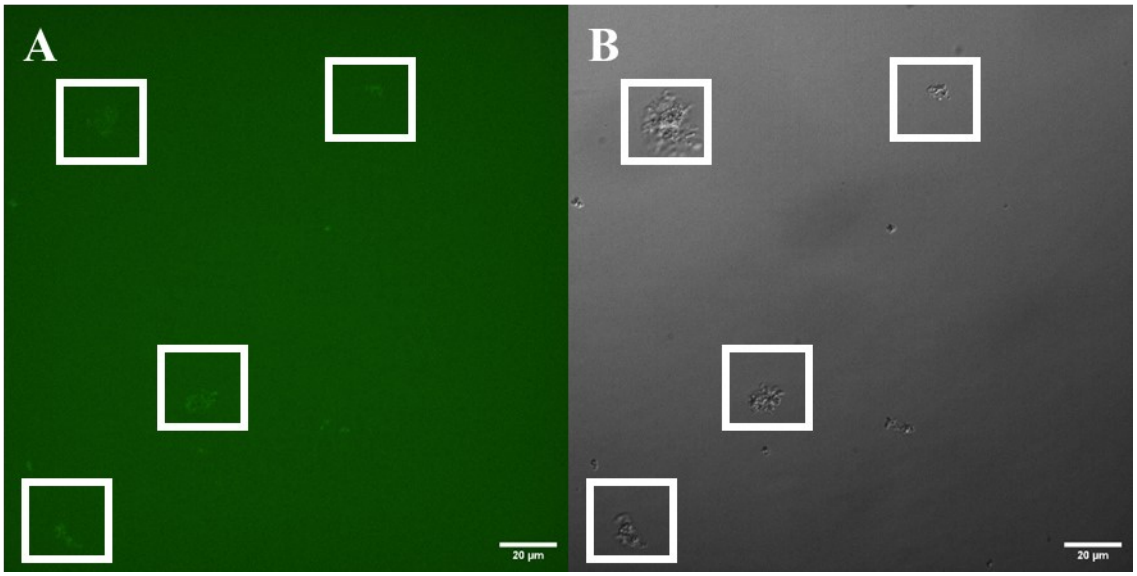

Fig. S18. Preliminary characterization via confocal microscopy under (A) fluorescence channel and (B) DIC channel of V8-pBFP-His, in the presence of the hydrophobic dye AZ488. Confocal microscopy was performed at 50°C with a peptide concentration of 500µM and AZ488 dye concentration of 0.2µg/mL, using the Dragonfly Confocal Microscope system. White boxes highlight that the particles observed under the DIC channel also present higher signal strength under the fluorescence channel, indicating the AZ488 accumulated inside these particles due to the present of hydrophobic phases.

ELP-BFP versatility (Fig. S19)

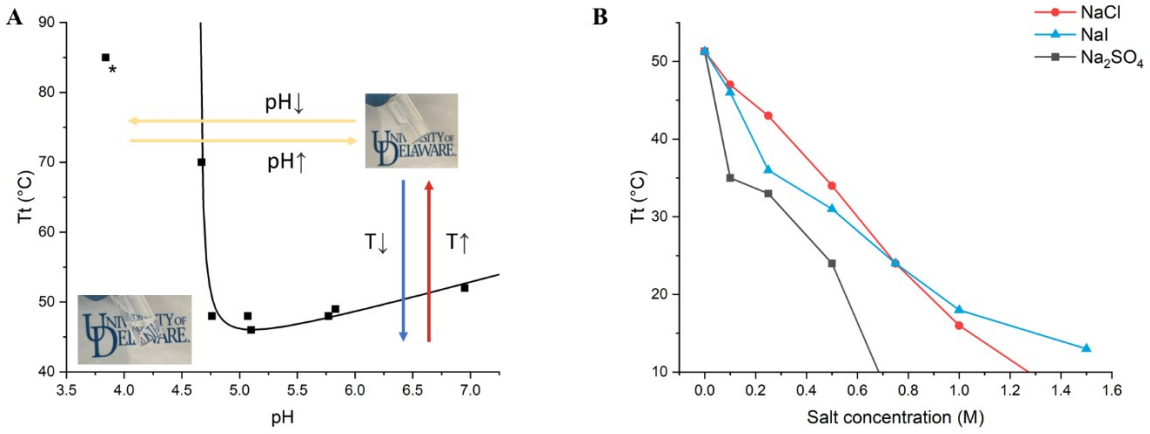

Fig. S19. Transition temperatures of V8-aBFP-His under different solution conditions. (A) pH responsiveness of V8-aBFP-His. The transition temperature of 500uM V8-aBFP-His in citric acid-sodium phosphate buffer at different pH highlights that the ELP-BFP system shows a sharp response to changes in pH. The inset pictures illustrate the phase transition under different stimuli. The position of the inset picture does not reflect the actual condition of solution. * The T_t at pH 3.85 was above 85°C. (B) Influence of various salts on the V8-pBFP-His transition temperature. The variations in transition temperature of 500uM V8-aBFP-His in pH=5.6 citric acid-sodium phosphate buffer with different salts indicates the possibility of further tuning transition temperature through variations in salt concentration.

The potential for pH-responsive transitions was assessed in experiments utilizing V8-aBFP-His since the transition temperature of V8-aBFP-His (ca. 45°C) is centrally located at accessible experimental temperatures (5°C to 85°C) (Figure S10a) and thus provides a wider range of variations in T_t with changes of pH. The V8-aBFP-His shows an expected minimum in the T_t near its isoelectric point (pI=5.21[6]), and then shows a sharp increase in T_t with decreasing pH (below pH 4.6), attributed to the increased charge of the aBFP sequence and of the histidine tag and confirms the expected pH-sensitivity of ELP-BFP amphiphiles. Our observations are consistent with previous studies that report a similar increase in T_t with decreased pH for histidine-containing ELPs ($(VPGVG(VPGHG)_4)_{16}$)[7] and for charged ELPs that contain a histidine tag.[8]

Many types of ELPs have been used in inverse transition cycle purification in which the phase transition can be triggered either by temperature or by salt concentration to separate a target protein from other contaminants;[9] multiple studies have also demonstrated the effect of salts on assembly kinetics and morphology.[10,11] Three different salts, Na_2SO_4, NaCl, and NaI, were therefore selected to assess T_t of the ELP-BFPs in salt solutions with different lyotropic properties.(Figure S10b) While the presence of any of these salts decreased the T_t for the V8-aBFP-His, the most kosmotropic ion SO_4^{2-} exhibited the strongest effect on T_t. The most chaotropic ion I^- should increase the T_t when compared to the effect of Cl^-, although this effect was only observed at high salt concentrations in the studies reported here. At low concentrations, I^- decreased the T_t to a greater extent than Cl^-, which may be a result of bridging between I^- and protonated histidine[12] that would serve to increase the interactions of the ELP domain. However, at high salt concentrations, the presence of additional I^- would disrupt the bridging interaction and increase the contribution of the mainly chaotropic effects of the I^-. The influence of salt on the T_t of the same ELP-

BFP sequence enables an alternative approach to tune the transition temperature of ELP-BFP and achieve assembly at lower temperatures.

References:

1 R. Chelli, F. L. Gervasio, P. Procacci and V. Schettino, *J. Am. Chem. Soc.*, 2002, **124**, 6133–6143.
2 L. H. Kapcha and P. J. Rossky, *J. Mol. Biol.*, 2014, **426**, 484–498.
3 J. R. McDaniel, D. C. Radford and A. Chilkoti, *Biomacromolecules*, 2013, **14**, 2866–2872.
4 Y. Li, D. R. Dautel, M. A. Gray, M. E. McKenna and J. A. Champion, *J. Mater. Chem. B*, 2023, **11**, 6443–6452.
5 J. Y. Su, R. S. Hodges and C. M. Kay, *Biochemistry*, 1994, **33**, 15501–15510.
6 PepCalc.com - Peptide calculator, https://pepcalc.com/, (accessed November 1, 2023).
7 D. J. Callahan, W. Liu, X. Li, M. R. Dreher, W. Hassouneh, M. Kim, P. Marszalek and A. Chilkoti, *Nano Lett.*, 2012, **12**, 2165–2170.
8 C.-Y. Lin and J. C. Liu, *J. Mater. Chem. B*, 2019, **7**, 5245–5256.
9 Y. Cho, Y. Zhang, T. Christensen, L. B. Sagle, A. Chilkoti and P. S. Cremer, *J. Phys. Chem. B*, 2008, **112**, 13765–13771.
10 D. R. Dautel and J. A. Champion, *Biomacromolecules*, 2021, **22**, 116–125.
11 J. T. Cirulis and F. W. Keeley, *Biochemistry*, 2010, **49**, 5726–5733.
12 G. Giester, V. V. Ghazaryan, M. Fleck, G. S. Tonoyan and A. M. Petrosyan, *J. Mol. Struct.*, 2019, **1182**, 317–326.